MATERIALS CHEMISTRY FRONTIERS

RESEARCH ARTICLE

View Article Online
View Journal | View Issue

Cite this: *Mater. Chem. Front.*, 2024, **8**, 3807

A polar multilayered two-dimensional hybrid perovskite for self-driven X-ray photodetection with a low detection limit†

Jingtian Zhang,[ab] Wuqian Guo,*[a] Haojie Xu,[a] Qingshun Fan,[a] Linjie Wei,[a] Xianmei Zhao,[a] Zhihua Sun *[a] and Junhua Luo [a]

Received 10th July 2024,
Accepted 17th September 2024

DOI: 10.1039/d4qm00582a

rsc.li/frontiers-materials

Recently, two-dimensional (2D) organic–inorganic hybrid perovskites (OIHPs) with the general chemical formula of $(A)_2(B)_{n-1}PbX_{3n+1}$ have garnered significant interest in optics and optoelectronics. Presently, the B-site cations in the perovskite cage are confined exclusively to small-size cations (such as Cs^+ and $CH_3NH_3^+$), while high-quality crystals of 2D OIHPs containing larger cations (*e.g.*, guanidinium, G^+) remain quite scarce for detecting X-ray application. Here, we have successfully fabricated a nanoGray-responsive self-driven X-ray detector using single crystals of a polar 2D hybrid perovskite, $IA_2GPb_2I_7$ (where IA is isoamylammonium), of which G cations are confined inside the perovskite cages. The dynamic freedom of IA^+ and G^+ organic cations' molecular movements supplies the impetus for the creation of electrical polarization. Upon X-ray radiation, a bulk photovoltaic voltage of 0.74 V is generated due to the spontaneous electric polarization, which affords the source for self-driven detection. The grown high-quality inch-size crystals show high resistivity (1.82×10^{10} Ω cm) and huge carrier migration lifetime product ($\mu\tau$ = 2.7×10^{-3} cm^{-2} V^{-1}). As expected, an X-ray detector fabricated on high-quality crystals enables dramatic X-ray detection performances under 0 V, boasting an excellent sensitivity of 115.43 μC Gy_{air}^{-1} cm^{-2} and an impressively low detection limit of 9.6 nGy_{air} s^{-1}. The detection limit is superior to many known perovskite X-ray detectors. The investigation focuses on the rational design and engineering of new hybrid perovskites toward high-demand self-powered X-ray detectors.

Introduction

2D hybrid perovskites have paramount significance in the field of optoelectronics, such as LEDs, solar cells, photodetectors, *etc.*[1–5] From a structural standpoint, organic components and inorganic frameworks feature an alternative arrangement, which lead to a significant modulation of electronic and optical properties.[6–9] In particular, the 2D quantum confinement phenomenon plays a pivotal role in enhancing the swift separation of photogenerated electron–hole pairs, while also boosting electron mobility, thereby reducing recombination rates significantly.[10,11] Hence, these inherently distinctive attributes render them promising candidates for the construction of a new conceptual optoelectronic apparatus. As an intriguing subclass, 2D Ruddlesden–Popper multilayered $(A)_2(B)_{n-1}PbX_{3n+1}$(where A and B are organic cations, X is a halogen group element)[12–14] have many particular advantages, such as the high atomic number of elements, high resistivity, prolonged carrier lifetime, and strong irradiation absorption ability.[15,16] These fascinating characters endow great application potential in the field of X-ray detectors. As an example, the study by Zhang *et al.* presented an X-ray detector employing the $BA_2MA_9Pb_{10}I_{31}$ single crystal, which has an extraordinary sensitivity of 8000 μC Gy_{air}^{-1} cm^{-2}.[17] Although the accomplishments in perovskite-based X-ray detection are impressive, these detectors are operated within substantial external electrical fields to effectuate the segregation and conveyance of electron–hole pairs, consequently yielding a bulky overall circuit and higher energy expenditure.[18,19] By contrast, the bulk photovoltaic effect (BPVE) refers to the electric current generation in a homogeneous material under light illumination.[20] It relates to spontaneous electric polarization in polar materials enabling the separation and transportation of photogenerated carriers along the polar orientation, which has been efficaciously employed in optoelectronic devices.[21] This approach potentially diminishes the detector's dark current, consequently enabling a

[a] *State Key Laboratory of Structural Chemistry, Fujian Institute of Research on the Structure of Matter, Chinese Academy of Sciences, Fuzhou, Fujian 350002, P. R. China. E-mail: sunzhihua@fjirsm.ac.cn*

[b] *School of Physical Science and Technology, ShanghaiTech University, Shanghai 201210, P. R. China*

† Electronic supplementary information (ESI) available. CCDC 2353249. For ESI and crystallographic data in CIF or other electronic format see DOI: https://doi.org/10.1039/d4qm00582a

lower detection limit.[22] In this context, investigating the application of hybrid perovskite in bulk photovoltaics in large-scale photovoltaics becomes crucial for improving self-powered X-ray detection systems.[23,24]

Recently, significant advancements have been attained in the realm of 2D hybrid perovskites through delicate manipulation of perovskite components, the improvement of crystal quality, and the implementation of precise surface treatments.[25–27] Nevertheless, the chemical modulation of structures primarily concentrates on the A-site organic constituents, while the B-site cations remain constrained by the tolerance-factor concept, for example, $CH_3NH_3^+$ (MA, $r \sim 217$ pm), $[CH(NH_2)_2]^+$ (FA, $r \sim 253$ pm), and $CH_3CH_2NH_3^+$ (EA, $r \sim 274$ pm). It remains challenging to alloy various B-site cations in the perovskite cavities. 2D Ruddlesden–Popper perovskites relax the constraint of the tolerance-factor concept, thus facilitating the incorporation of large B-site cations. The fascinating attributes of the guanidinium cation $(C(NH_2)_3^+$, G^+, $r \sim 278$ pm) are the formation of strong hydrogen bonds and high alkalinity ($pK_a = 13.6$), which increases the polarity of the perovskites with G^+ cations introduced.[28–30] In addition, G^+ cations can form hydrogen bindings with inorganic PbI_6 octahedra, thereby bolstering the rigidity of the cubic surface structure. A stabilized rigidity lattice structure should have a lower defect formation energy, which will facilitate the charge carrier collection process.[31] Despite great efforts devoted to this family, there are few studies on their X-ray detection properties. It is imperative to explore the viability of G^+ cations as B-site cations in perovskite cages for the creation of innovative 2D hybrid perovskite structures, and the development of a self-driven X-ray detector.

In this work, we accomplish the innovative integration of a new polar multilayer hybrid perovskite $IA_2GPb_2I_7$ (IAG, IA = isoamylammonium), achieved by integrating G^+ cations into the structurally distorted cage formed by PbI_6 octahedra. Due to the spontaneous electric polarization, a bulk photovoltaic voltage of 0.74 V is created under X-ray illumination, which affords the source for self-driven detection. In combination with large resistivity and huge carrier migration lifetime product ($\mu\tau$), the crystal-based detector of 1 shows dramatic X-ray detection performances, including an excellent sensitivity of 115.43 μC Gy_{air}^{-1} cm^{-2} and an exceedingly low detection limit of 9.6 nGy_{air} s^{-1} at 0 V. We believe this study underscores the untapped potential of $IA_2GPb_2I_7$ in terms of X-ray detector and paves the way to devise novel possibilities for further self-driven X-ray detection.

Experimental section

Synthesis of crystals

Add lead acetate trihydrate, isoamylamine, and $[C(NH_2)_3]_2CO_3$ to the HI solution at a stoichiometric ratio of 2 : 2 : 1 and heat to boiling under steady magnetic stirring. Upon achieving a pellucid yellow solution, discontinue both heating and stirring. Proceed with a cooling technique to grow large red crystals. The cooling rate is 0.5 °C d^{-1}. Rectangular red single crystals with the largest size of up to 11 × 30 × 0.3 mm^3 were harvested after several days. The pristine crystals were wiped and dried in an N_2 glovebox overnight and then annealed at 343 K for 2 h to completely remove moisture and release lattice stress.

Characterization of $IA_2GPb_2I_7$

Powder X-ray diffraction (PXRD) patterns were procured using a Rigaku Miniflex 600 X-ray diffractometer, covering a 2θ range from 5° to 40° with a step increment of 0.02°. A PerkinElmer Lambda 950 UV-vis-IR spectrophotometer was utilized for conducting UV-vis spectrometry. Variable-temperature conductivity measurements were executed through a direct-current two-terminal technique, spanning a temperature range of 350 to 400 K. The thermogravimetric analysis was executed by the STA449C Thermal Analyser.

Morphology characterization

Surface observations of **IAG** were carried out using a Bruker Dimension ICON atomic force microscope for atomic force microscopy (AFM) imaging and a JEOL JSM6700-F field emission scanning electron microscope for scanning electron microscopy (SEM) analysis.

Single-crystal structure determination

Mo Kα radiation ($\lambda = 0.77$ A) single crystal X-ray diffraction on a Bruker D8 Quesr/Venture diffractometer. Using the SHELXTL program, the direct approach was used to resolve the crystal structure, and the full matrix technique based on F^2 was used to refine it. All crystallographic data were uploaded to the Cambridge Crystallographic Data Center (CCDC) with numbers 2353249.†

X-Ray detection

The current–voltage (I–V) traces and current–time (I–t) characteristics of the **IAG** device were recorded utilizing a high-precision Keithley 6517B electrode system. A silver-targeted Amptek Mini-X2 X-ray tube, capable of reaching a maximum power output of 4 W, served as the radiation source. The upper limit for X-ray photon energy reached 50 keV, with a prominent intensity peak at 22 keV. The modulation of the X-ray tube's dose rate was accomplished through varying its tube current, subsequently undergoing measurement.

Results and discussion

The red flaky crystal measuring 11 × 30 × 0.3 mm^3 in dimensions was acquired through temperature-controlled cooling techniques (Fig. 1a). The PXRD pattern recorded at 298 K distinctly verifies the phase purity of the as-grown crystal. Periodical diffraction peaks correspond to (h00) series of the reflections, revealing the perfect crystal orientation (Fig. 1b and Fig. S1, ESI†). The atomic force microscopy (AFM) and scanning electron microscopy (SEM) images corroborate this fact (Fig. S2 and S3, ESI†). The PXRD patterns placed for 6 months are consistent with that of the fresh crystal, indicating excellent environmental stability of **IAG** (Fig. S4, ESI†). Fig. 1c depicts second harmonic generation (SHG) signals of 1 is

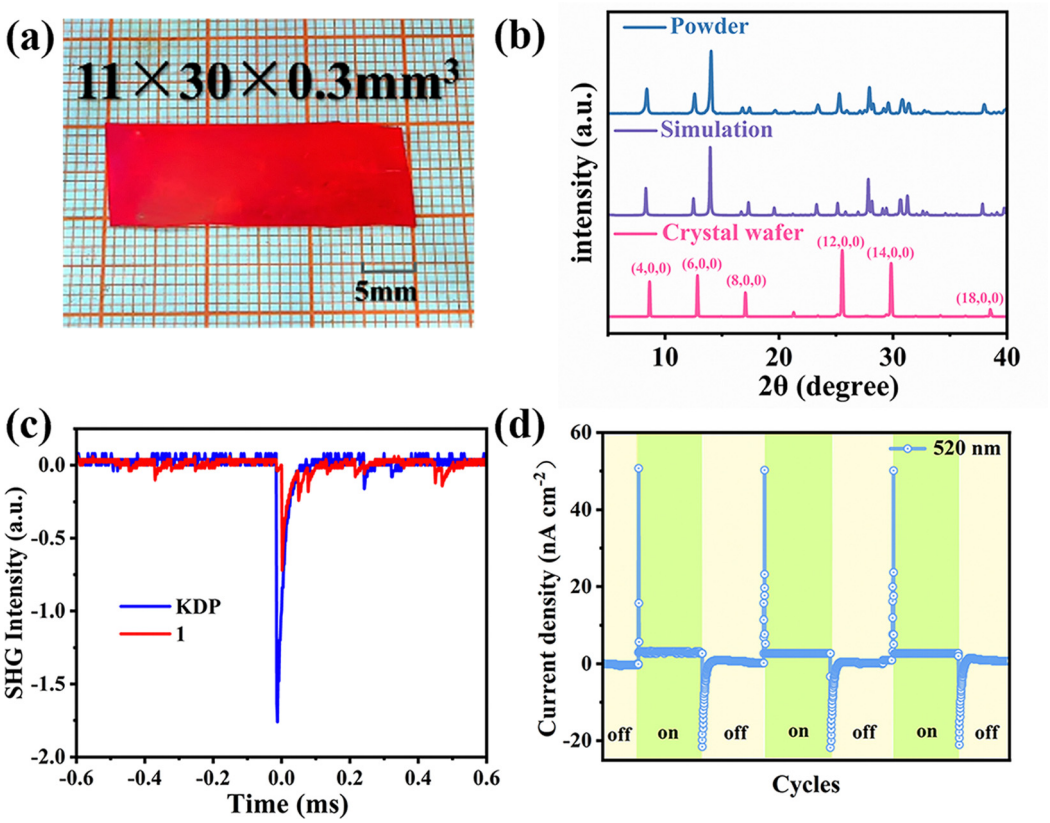

Fig. 1 (a) The photo of single crystals of **IAG**. (b) The XRD measurement of powder and bulk crystals. (c) The comparison of SHG signals of **IAG** and KDP. (d) Photoresponse behavior of **IAG** under 520 nm laser illumination with 0 V bias.

approximately 0.42 times the intensity of KDP's, indicating the non-centrosymmetric structure of the compound. Photopyroelectric currents serve as compelling evidence for a polar structure. The sharp photopyroelectric current peaks can be observed at room temperature (Fig. 1d), suggesting a possible polar structure of **IAG**.

Single-crystal structural analyses reveal that **IAG** crystallizes in the orthorhombic space group $Cmc2_1$ at room temperature, and the polar axis is along the *c*-axis (Fig. 2a, Tables S1, S2, and S3, Fig. S5, ESI†). Within this framework, edge-sharing PbI_6 octahedra form an inorganic network, with G^+ cations occupying the interstitial spaces (Fig. 2b). Benefiting from the large ionic radius of guanidine, the Pb–I–Pb angle of **IAG** (170°–175°) is less distorted than that of $MAPbI_3$ (163°–179°) (Fig. S6 and Tables S4, ESI†). Reduced lattice distortion is conducive to the improvement of charge transport efficiency and the realization of high-performance.

optoelectronic response. Insights from Hirshfeld surface analyses reveal that the organic cations G^+ interact with the inorganic frameworks through robust hydrogen bonding interactions. And the strong N–H···I contact is distributed over 53.4% of the surface area (Fig. S7 and Tables S5, ESI†). The increased intensity of hydrogen bonds contributes significantly to the lattice rigidity and structural stability, ultimately leading to enhanced performance in X-ray detection capabilities. An arrangement for **IAG** akin to a 2D quantum-confinement architecture is presented, which features alternating layers of organic cation bilayers and inorganic perovskite sheets. Here, the inorganic part serves as the "well" and the organic part behaves as the "barrier". Specifically, the bilayered organic IA^+ cations are directionally arranged between the nearby inorganic perovskite layers. Especially, the molecular dipole moment calculated by the point charge model is ~15.93 Debye along the polar *c*-axis direction, which strongly supports the formation of a polar structure and the electric polarization of **IAG** (Table S6, ESI†).

The examination of the optical absorption properties for **IAG** was conducted through UV-visible diffuse reflectance spectroscopy, from which the optical bandgap was calculated using the Tauc curve. As depicted in Fig. 3a, a distinct absorption edge at 609 nm is observed, corresponding to an optical bandgap (E_g) of 2.03 eV. Further insights into the electronic structures, derived from first-principles density functional theory, confirm the direct nature of the bandgap, as evidenced by the positions of the conduction band minimum (CBM) and valence band maximum (VBM). The computed band gap energy amounts to 2.00 eV, consistent with experimental findings (Fig. 3b).[32,33] This figure aligns within the spectrum of bandgap values observed in various lead iodide hybrid perovskites, such as $(PA)_2(G)Pb_2I_7$ (2.02 eV),[34] $(2IPA)_2FAPb_2I_7$ (2.03 eV),[35] $(BA)_2(FA)Pb_2I_7$ (2.03 eV),[36] *etc.* Moreover, partial density of states (PDOS) indicates that the inorganic layer plays a dominant role in the bandgap (Fig. 3c). Specifically, the VBM is contributed by I-5p orbitals while the CBM

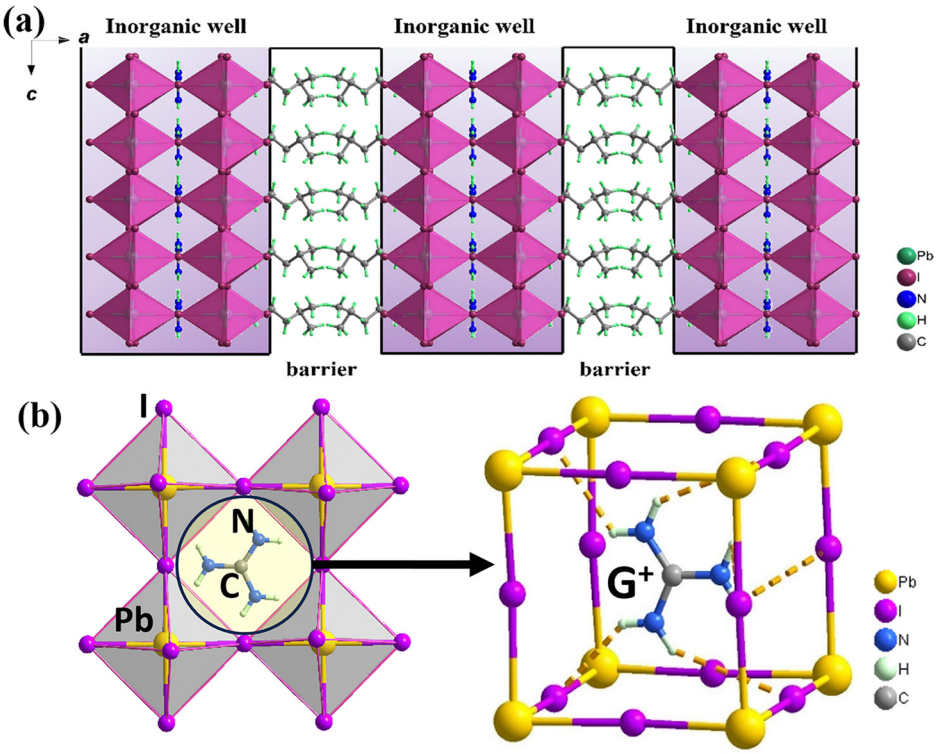

Fig. 2 (a) Structural configuration of **IAG** that appeared as the 2D perovskite quantum-confined motif. (b) IA^+ cations bound to PbI_6 octahedra through N–H···I hydrogen bonds, as shown by the dashed lines.

mainly originates from Pb-6p states. High resistivity is beneficial for the device to suppress noise and improve the detection limit. The resistivity of **IAG** could be calculated as 1.82×10^{10} Ω cm along the *c*-axis direction (Fig. 3d), which is much better than conventional 3D hybrid perovskites, including $MAPbX_3$[37–39] (X = Cl, Br, I; 10^7–10^8 Ω cm).

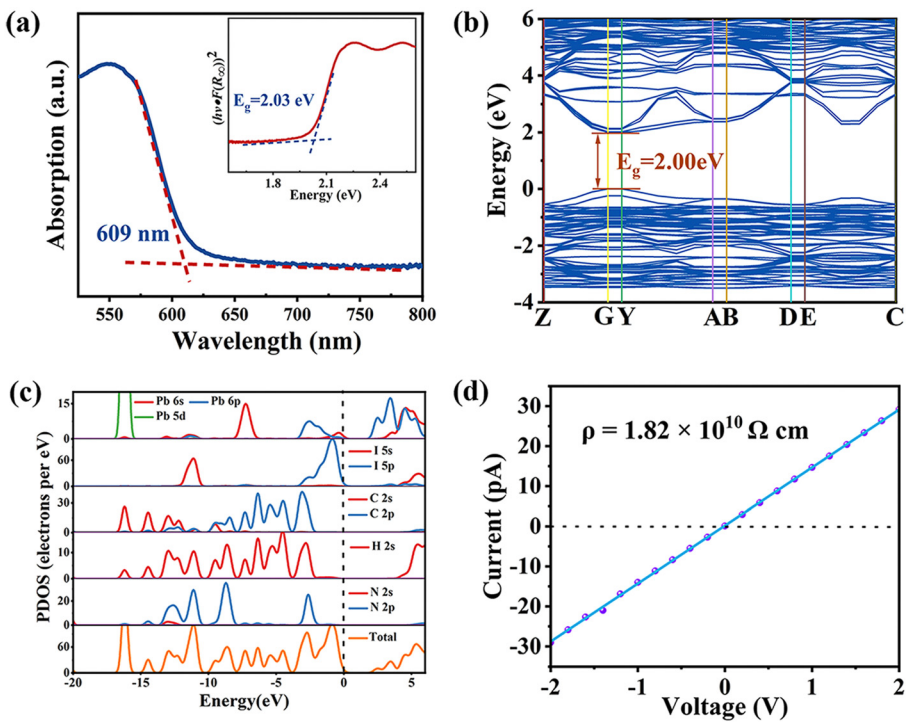

Fig. 3 (a) Absorption spectra of **IAG** (inset: the calculated band gap). (b) The band structure. (c) Partial density of states of **IAG.** (d) Bulk resistivity of **IAG**.

For the realization of direct X-ray detection, it's crucial that X-ray photons are absorbed entirely within the active material layer. According to the NIST's XCOM database, the computed absorption coefficient for **IAG** surpasses that of Si and is equivalent to α-Se and CsI (Fig. 4a). Meanwhile, when the crystal thickness reaches 1.5 mm, **IAG** can effectively attenuate almost 100% of X-ray photons, which is beneficial to X-ray detection (Fig. 4b). As illustrated in Fig. 4c, the construction of devices with electrodes in a direction parallel to the *c*-axis is fabricated to evaluate the charge transport performance of **IAG**. The carrier mobility-lifetime ($\mu\tau$) product is computed by the modified Hecht equation:[40]

$$I = \frac{I_0 \mu\tau V}{L^2}\left[1 - \exp\left(-\frac{L^2}{\mu\tau V}\right)\right]$$

where I_0 is saturation photocurrent, V represents the imposed voltage and L indicates the electrode separation. The $\mu\tau$ product of **IAG** under X-ray illumination was calculated as 2.7×10^{-3} cm^{-2} V^{-1} (Fig. 4d), which is higher than that of the commercial α-Se film ($\approx 10^{-7}$ cm^2 V^{-1})[41] and the $MAPbI_3$ polycrystalline film (2×10^{-7} cm^2 V^{-1}).[42] An elevated $\mu\tau$ product signifies an extended average carrier transport distance, thereby enhancing the effectiveness of charge accumulation. The harmonious combination of huge bulk resistivity, substantial $\mu\tau$-product, and robust X-ray attenuation endows **IAG** with extensive application prospects in terms of direct X-ray detection.

Given the polar structure exhibited by **IAG** at room temperature, an evident BPVE along the polarization axis is the anticipated direction under X-ray illumination. As shown in Fig. 5a and b, **IAG** demonstrates a robust BPVE along the *c*-axis with a 0.74 V open-circuit photovoltage and exhibits excellent photoactive stability. By combining strong BPVE, we envision the significant potential for **IAG** has great potential in high-capability self-driven X-ray detectors. Consequently, we proceeded to investigate the X-ray detection capabilities of the **IAG** detector in detail. With increasing X-ray dose rates, the photocurrent density rises almost linearly (Fig. 5c). Sensitivity (S) is a key index of the response performance of the reaction detector to X-ray irradiation and can be calculated using the formula:

$$S = \frac{J_{photo} - J_{dark}}{D}$$

where J_{photo} and J_{dark} are the current density under X-ray irradiation and in darkness, respectively. Additionally, D signifies the X-ray dose rate. An impressive detector sensitivity of 115.43 μC Gy_{air}^{-1} cm^{-1} is obtained, surpassing that of conventional materials, for example, Si (8 μC Gy_{air}^{-1} cm^{-2} under 0.5 V μm^{-1}),[43] α-Se (20 μC Gy_{air}^{-1} cm^{-2} under 2000 V),[44] and GaN p–n diodes (20 μC Gy_{air}^{-1} cm^{-2} under 0 V).[45] Furthermore, the **IAG** detector exhibits exceptional responsiveness when subjected to escalating X-ray dose rates under additional bias. Upon increasing the external voltage to 80 V, the **IAG** detector demonstrates a remarkable sensitivity up to 2222.23 μC Gy_{air}^{-1} cm^{-2}, which can be ascribed to the enhanced charge collection efficiency in the presence of stronger external electric fields (Fig. 5d). The assessment of an X-ray detector's performance significantly involves the determination of its detection limit, delineated by the signal-to-noise ratio (SNR). This crucial value is

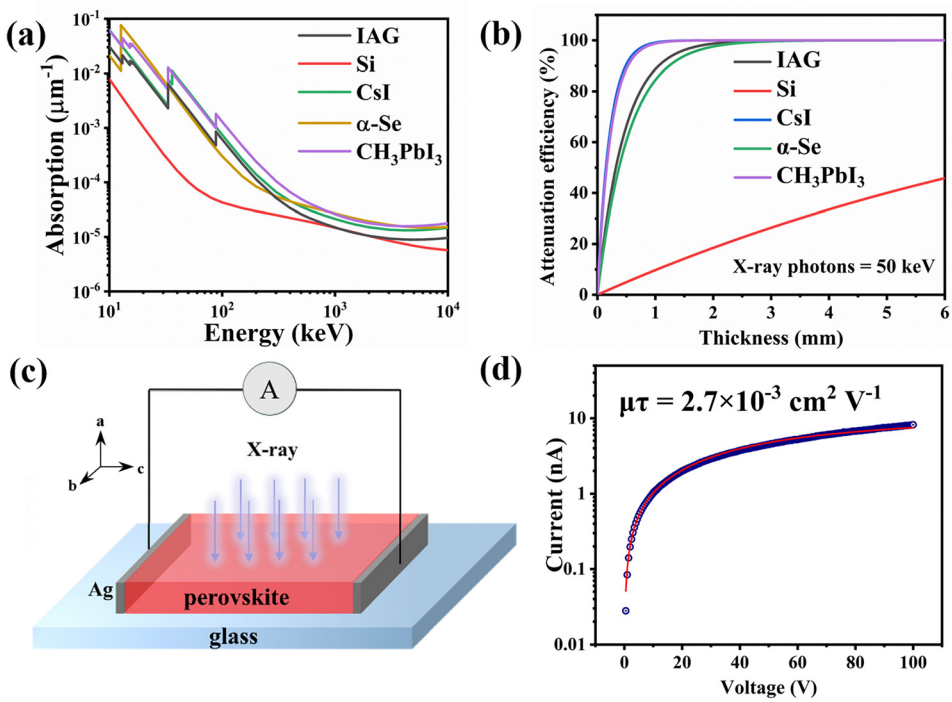

Fig. 4 (a) Absorption coefficients of **IAG**, Si, CsI, α-Se, and $MAPbI_3$ as a function of photon energy. (b) Attenuation efficiency of 50 keV X-rays on **IAG**, Si, CsI, α-Se, and $MAPbI_3$ with different thicknesses. (c) Structural diagram of direct X-ray detector made of **IAG**. (d) Photoconductivity measurement of **IAG**.

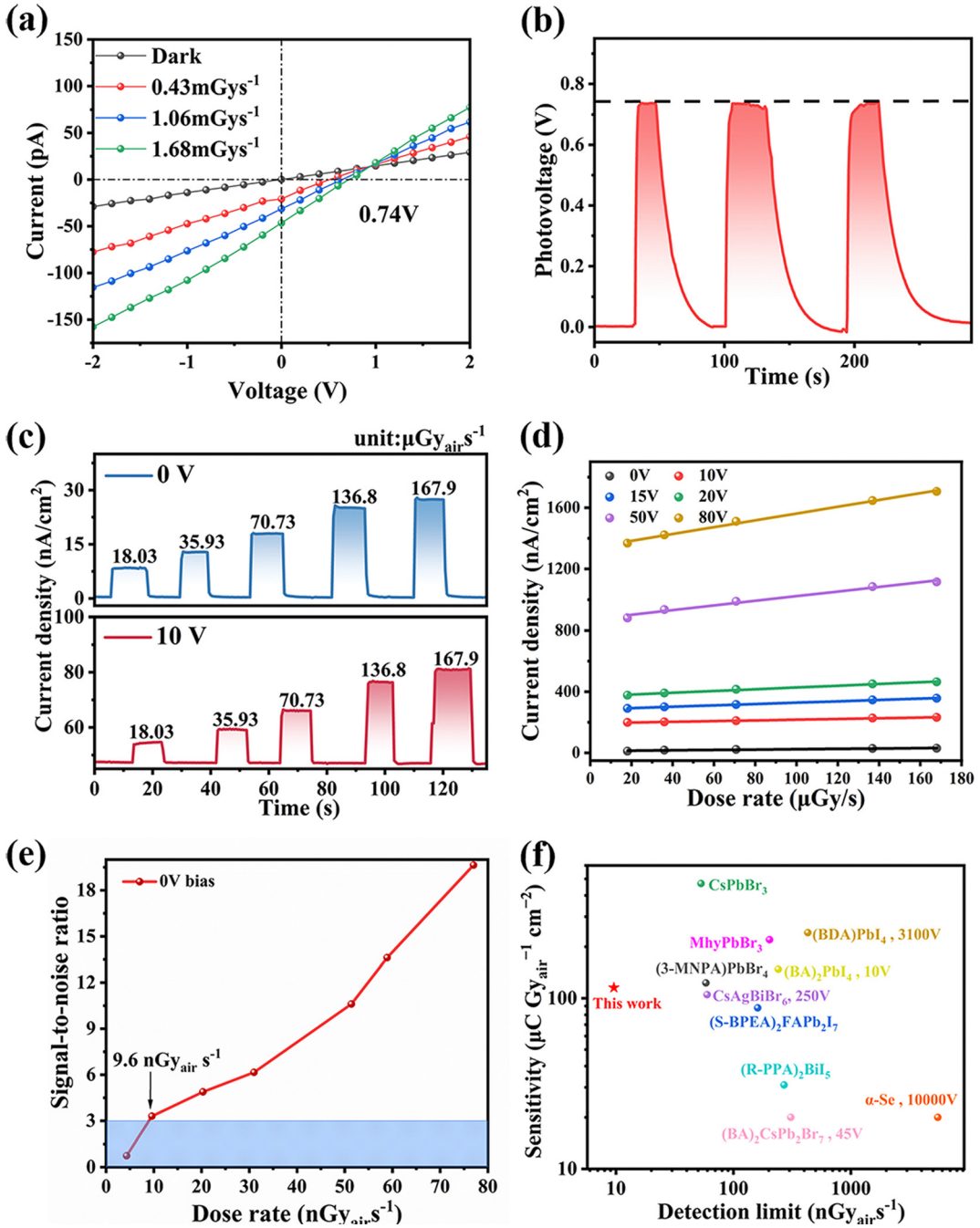

Fig. 5 (a) The radiation photovoltaic of **IAG**. (b) Time-dependent photocurrent on/off switching under X-ray. (c) X-ray response under different dose rates at 0 V and 10 V bias. (d) The photocurrent density under different applied voltages and different dose rates. (e) SNR of **IAG** at 0 V. (f) Summarized sensitivity and detection limit of some representative SC devices (The crystal material marked with the operating voltage in the figure are conventional commercial detectors, others are self-driven detectors that have been reported.).

approximated utilizing the following equation:

$$\mathrm{SNR} = \frac{I_{\mathrm{photo}} - I_{\mathrm{dark}}}{\sqrt{\frac{1}{N}\sum_{\mathrm{i}}^{n}\left(I_{\mathrm{i}} - I_{\mathrm{photo}}\right)^2}}$$

where I_{i} is the photocurrent, I_{photo} is the average response current under X-ray irradiation, and I_{dark} is the average dark current. The ascertainable dose rate, denoted by SNR $\geq$ 3, is delineated as the detection limit. Strikingly, the SNR of 3.3 is achieved under an extremely small X-ray dose rate of 9.6 $\mathrm{nGy_{air}\ s^{-1}}$(Fig. 5e and Fig. S8, ESI†), which is 1/500 of the dose rate of 5.5 $\mathrm{\mu Gy_{air}\ s^{-1}}$ typically utilized for medical imaging purposes. Such a low detection limit is much better than most known perovskite X-ray detectors (Fig. 5f and Table S7, ESI†). Such an ultralow detection limit is mainly attributed to the high bulk resistance and splendid quality single crystal of **IAG**.

In the detector, ion migration could increase the current drift, which will affect the detection limit of the detector.[46,47] The assessment of activation energy (E_a) of ion migration in **IAG** was carried out through the examination of the temperature-dependent conductivity, which is calculated using

$$\sigma(T) = \frac{\sigma_0}{T}\exp\left(\frac{-E_a}{k_B T}\right)$$

where σ is the conductivity at the corresponding temperature, σ_0 is the constant, and k_B is the Boltzmann's constant. The conductivity of **IAG** displays an ascending trend with a temperature rise, undergoing a distinct transition from electron-dominated conductivity to ion-dominated conductivity at precisely 386.1 K. And the conductivity.

changes sharply from electron conductivity to ion conductivity at 386.1 K. The E_a calculated by fitting $\ln(\sigma T)$ *vs.* $(1000/T)$ curve is 1.58 eV (Fig. 6a), which is superior to three-dimensional perovskite, including $MAPbI_3$ (E_a = 0.984 eV)[48] and $MAPbBr_3$ (E_a = 0.168 eV).[49] It proves that the conductivity of IAG is mainly due to electron conduction below 386.1 K, and ion migration is inhibited.[50] The photodetector's responsiveness to light, denoted by the response time (τ) is another crucial factor for a photodetector which reveals rising and falling components of response time (τ_{rise}/τ_{fall}). Rise time refers to the time required for the obtained stable signal to rise by 10% to 90%, and decay time refers to the time required for the signal to decrease from 90% to 10%. Notably, both the τ_{rise} is assessed to be 280 ms and τ_{fall} is assessed to be 170 ms deduced within a single cycle (Fig. 6b). 2D hybrid perovskites exhibit unparalleled stability in terms of phase stability, a characteristic that significantly enhances their potential for expanding device applications. As shown in Fig. 6c, under the irradiation of X-ray for about 100s twice, the photocurrent has not attenuated obviously. In Fig. 6d, it is depicted that the photocurrent exhibits negligible variation under X-rays with a dose rate of 144.8 μGy s^{-1} and a total dose of 11.67 mGy, thereby indicating great stability of the detector during operational conditions. In addition, we performed a long-term tracking measurement on IAG under ambient conditions without any encapsulation, and the result shows that IAG has phase stability, and the response current of the detector still maintained 83.7% of the initial value after 30 days (Fig. S9, ESI†). All of these survey results indicate that IAG holds considerable potential as a prospective candidate for excelling in photodetector applications.

Conclusions

Conclusively, through alloying the cage-templated moiety of large-size G^+ cations, we efficaciously assembled one kind of

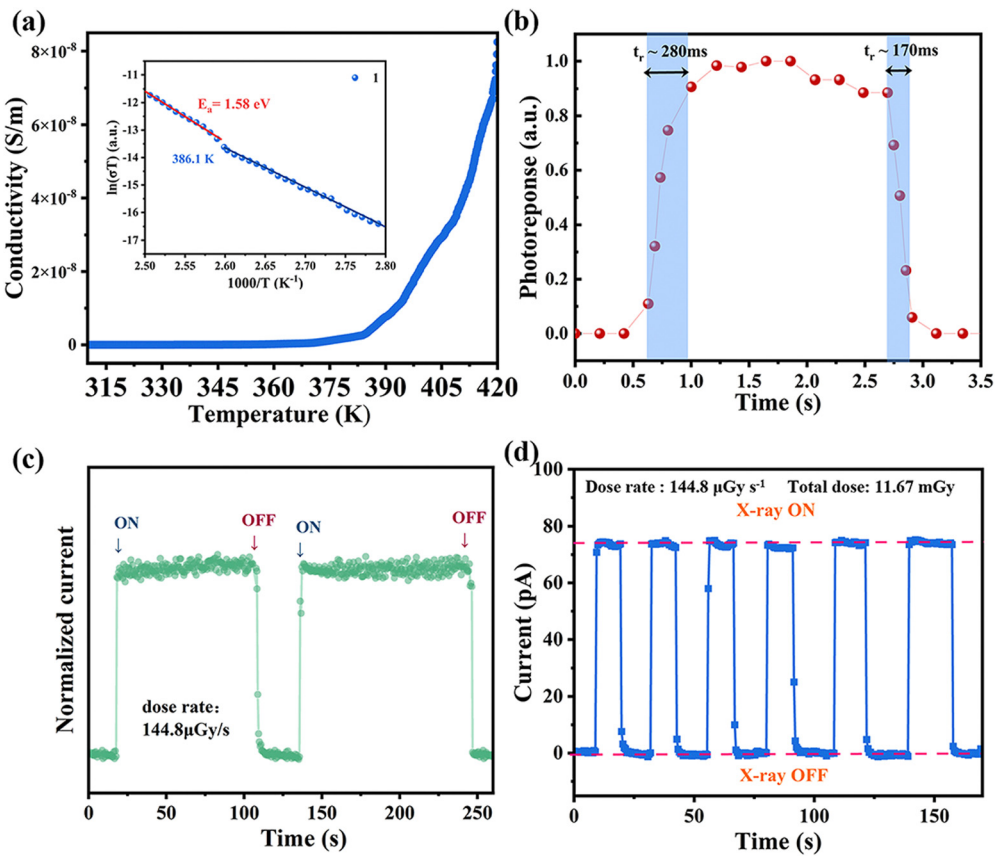

Fig. 6 (a) The temperature-dependent conductivity of **IAG** (Inset: The assessment of activation energy (E_a) of ion migration in **IAG**). (b) Temporal measurements of the photocurrent during the cycle. (c) Photocurrent stability of **IAG** under continuous X-ray irradiation. (d) Reduplicative switching cycles of photoresponse of the installation to X-ray radiation.

new 2D multilayer hybrid perovskite $IA_2GPb_2I_7$ for nanoGray-responsive self-driven X-ray photodetection. The dynamic freedom of IA^+ and G^+ organic cations' molecular movements provides the impetus for the creation of electrical polarization. Upon X-ray illumination, the bulk photovoltaic voltage of 0.74 V supported by spontaneous polarization affords the source for self-driven detection. Based on high resistivity (1.82×10^{10} Ω cm) and huge carrier migration lifetime product ($\mu\tau = 2.7 \times 10^{-3}$ cm^{-2} V^{-1}) of **IAG**, X-ray detectors fabricated on superior quality crystals exhibit remarkable X-ray detection performance under zero bias with an excellent sensitivity of 115.43 μC Gy_{air}^{-1} cm^{-2} and the exceedingly low detection limit of 9.6 nGy_{air} s^{-1}. As far as we know, such a detection limit outperforms many reported perovskite detectors. Not only will this study pave the pathway for the reasonable design of novel candidates in the 2D material family, but it will also prove prospects for high-performance self-powered X-ray detection.

Author contributions

J. Zhang synthesized and characterized the perovskite materials. W. Guo and H. Xu performed the calculations and analyses. Q. Fan determined the single-crystal structure. W. Lin and X. Zhao performed the characterization of the detector device. J. Luo provided suggestions for research. Z. Sun designed and directed the studies. J. Zhang and Z. Sun wrote the manuscript. All of the authors discussed the results and reviewed the manuscript.

Data availability

Crystallographic data for IAG has been deposited at the CCDC under 2353249 and can be obtained from **https://www.ccdc.cam.ac.uk/structures/ccdc-check=d8a60ac420c881b345ac5337e815a49a**.

Conflicts of interest

There are no conflicts to declare.

Acknowledgements

This work was supported by NSFC (22125110, U23A2094, 22305248 and U21A2069), the Natural Science Foundation of Fujian Province (2023J02028), the Postdoctoral Fellowship Program of CPSF under Grant Number GZB20240746, and the China Postdoctoral Science Foundation (2024T170923, 2024M753233, 2022TQ0337 and 2023M733497).

Notes and references

1 S. Han, M. Li, Y. Liu, W. Guo, M.-C. Hong, Z. Sun and J. Luo, Tailoring of a visible-light-absorbing biaxial ferroelectric towards broadband self-driven photodetection, *Nat. Commun.*, 2021, **12**, 284.
2 Y. Liu, S. Han, J. Wang, Y. Ma, W. Guo, X.-Y. Huang, J.-H. Luo, M. Hong and Z. Sun, Spacer Cation Alloying of a Homoconformational Carboxylate trans Isomer to Boost in-Plane Ferroelectricity in a 2D Hybrid Perovskite, *J. Am. Chem. Soc.*, 2021, **143**, 2130–2137.
3 Y. Ma, J. Wang, Y. Liu, S. Han, Y. Li, Z. Xu, W. Guo, J. Luo, M. Hong and Z. Sun, High performance self-powered photodetection with a low detection limit based on a two-dimensional organometallic perovskite ferroelectric, *J. Mater. Chem. C*, 2021, **9**, 881–887.
4 J. Wang, Y. Liu, S. Han, Y. Ma, Y. Li, Z. Xu, J. Luo, M. Hong and Z. Sun, Ultrasensitive polarized-light photodetectors based on 2D hybrid perovskite ferroelectric crystals with a low detection limit, *Sci. Bull.*, 2021, **66**, 158–163.
5 W. Guo, H. Chen, X. Liu, Y. Ma, J. Wang, Y. Liu, S. Han, H. Xu, J. Luo and Z. Sun, Rational alloying of secondary and aromatic ammonium cations in a metal-halide perovskite toward crystal-array photodetection, *Sci. China Mater.*, 2022, **65**, 179–185.
6 J. C. Blancon, H. Tsai, W. Nie, C. C. Stoumpos, L. Pedesseau, C. Katan, M. Kepenekian, C. M. M. Soe, K. Appavoo, M. Y. Sfeir, S. Tretiak, P. M. Ajayan, M. G. Kanatzidis, J. Even, J. J. Crochet and A. D. Mohite, Extremely efficient internal exciton dissociation through edge states in layered 2D perovskites, *Science*, 2017, **355**, 1288–1292.
7 X. Hong, T. Ishihara and A. V. Nurmikko, Dielectric confinement effect on excitons in PbI_4 -based layered semiconductors, *Phys. Rev. B: Condens. Matter Mater. Phys.*, 1992, **45**, 6961–6964.
8 H. Tsai, W. Nie, J.-C. Blancon, C. C. Stoumpos, R. Asadpour, B. Harutyunyan, A. J. Neukirch, R. Verduzco, J. J. Crochet, S. Tretiak, L. Pedesseau, J. Even, M. A. Alam, G. Gupta, J. Lou, P. M. Ajayan, M. J. Bedzyk, M. G. Kanatzidis and A. D. Mohite, High-efficiency two-dimensional Ruddlesden–Popper perovskite solar cells, *Nature*, 2016, **536**, 312–316.
9 Y. Liao, H. Liu, W. Zhou, D. Yang, Y. Shang, Z. Shi, B. Li, X. Jiang, L. Zhang, L. N. Quan, R. Quintero-Bermudez, B. R. Sutherland, Q. Mi, E. H. Sargent and Z. Ning, Highly Oriented Low-Dimensional Tin Halide Perovskites with Enhanced Stability and Photovoltaic Performance, *J. Am. Chem. Soc.*, 2017, **139**, 6693–6699.
10 S. Han, Y. Yao, X. Liu, B. Li, C. Ji, Z. Sun, M. Hong and J. Luo, Highly Oriented Thin Films of 2D Ruddlesden-Popper Hybrid Perovskite toward Superfast Response Photodetectors, *Small*, 2019, **15**, 1901194.
11 C. Katan, N. Mercier and J. Even, Quantum and Dielectric Confinement Effects in Lower-Dimensional Hybrid Perovskite Semiconductors, *Chem. Rev.*, 2019, **119**, 3140–3192.
12 S. N. Ruddlesden and P. Popper, New compounds of the K_2NIF_4 type, *Acta Cryst.*, 1957, **10**, 538–539.
13 S. N. Ruddlesden and P. Popper, On the crystal structure of the nitrides of silicon and germanium, *Acta Cryst.*, 1958, **11**, 465–468.
14 J. Calabrese, N. L. Jones, R. L. Harlow, N. Herron, D. L. Thorn and Y. Wang, Preparation and characterization of layered lead halide compounds, *J. Am. Chem. Soc.*, 1991, **113**, 2328–2330.

15 H. Wei, Y. Fang, P. Mulligan, W. Chuirazzi, H.-H. Fang, C. Wang, B. R. Ecker, Y. Gao, M. A. Loi, L. Cao and J. Huang, Sensitive X-ray detectors made of methylammonium lead tribromide perovskite single crystals, *Nat. Photonics*, 2016, **10**, 333–339.

16 J. Zhao, L. Zhao, Y. Deng, X. Xiao, Z. Ni, S. Xu and J. Huang, Perovskite-filled membranes for flexible and large-area direct-conversion X-ray detector arrays, *Nat. Photonics*, 2020, **14**, 612–617.

17 M. Zhang, L. Lei, W. Zhao, D. Yang, X. Zheng and W.-H. Zhang, Sensitive and Stable Ruddlesden–Popper Perovskite X-ray Detectors via Defect Passivation, *J. Phys. Chem. C*, 2023, **127**, 16219–16226.

18 X. Hu, H. Xu, Y. Liu, L. Lu, W. Guo, S. Han, J. Luo and Z. Sun, Incorporating an Aromatic Cationic Spacer to Assemble 2D Polar Perovskite Crystals toward Self-Powered Detection of Quite Weak Polarized Light, *J. Phys. Chem. Lett.*, 2022, **13**, 6017–6023.

19 H. Xu, F. Sun, W. Guo, S. Han, Y. Liu, Q. Fan, L. Tang, W. Liu, J. Luo and Z. Sun, Building Block-Inspired Hybrid Perovskite Derivatives for Ferroelectric Channel Layers with Gate-Tunable Memory Behavior, *Angew. Chem., Int. Ed.*, 2023, **62**, e202309416–e202309416.

20 W. Kraut and R. von Baltz, Anomalous bulk photovoltaic effect in ferroelectrics: A quadratic response theory, *Phys. Rev. B: Condens. Matter Mater. Phys.*, 1979, **19**, 1548–1554.

21 Q. Guan, H. Ye, S. You, Z.-K. Zhu, H. Li, X. Liu and J. Luo, Radia-tion Photovoltaics in a 2D Multilayered Chiral-Polar Halide Perov-skite toward Efficient Self-Driven X-Ray Detection, *Small*, 2024, **20**, 2307908.

22 C. Ji, Y. Li, X. Liu, Y. Wang, T. Zhu, Q. Chen, L. Li, S. Wang and J. Luo, Monolayer-to-Multilayer Dimensionality Reconstruction in a Hybrid Perovskite for Exploring the Bulk Photovoltaic Effect Enables Passive X-ray Detection, *Angew. Chem., Int. Ed.*, 2021, **60**, 20970–20976.

23 Z. Gou, W. Liu, S. Huanglong, X. Zhu, H. Sun, D. Yang and P. Wangyang, Self-Powered X-Ray Photodetector Based on Ultrathin PbI_2 Single Crystal, *IEEE Electron Device Lett.*, 2019, **40**, 578–581.

24 S. You, Z. K. Zhu, S. Dai, J. Wu, Q. Guan, T. Zhu, P. Yu, C. Chen, Q. Chen and J. Luo, Inch-Size Single Crystals of Lead-Free Chiral Perovskites with Bulk Photovoltaic Effect for Stable Self-Driven X-Ray Detection, *Adv. Funct. Mater.*, 2023, **33**, 2303523.

25 D. A. Egger, A. Bera, D. Cahen, G. Hodes, T. Kirchartz, L. Kronik, R. Lovrincic, A. M. Rappe, D. R. Reichman and O. Yaffe, What Remains Unexplained about the Properties of Halide Perovskites?, *Adv. Mater.*, 2018, **30**, 1800691.

26 N. P. Gallop, O. Selig, G. Giubertoni, H. J. Bakker, Y. L. A. Rezus, J. M. Frost, T. L. C. Jansen, R. Lovrincic and A. A. Bakulin, rotational cation dynamics in metal halide perovskites: effect on phonons and material properties, *J. Phys. Chem. Lett.*, 2018, **9**, 5987–5997.

27 L. M. Herz, How lattice dynamics moderate the electronic properties of metal-halide perovskites, *J. Phys. Chem. Lett.*, 2018, **9**, 6853–6863.

28 T. Ishikawa, *Superbases for Organic Synthesis: Guanidines, Amidines, Phosphazenes and Related Organocatalysts*, John Wiley & Sons, Inc., 2009.

29 F. V. Drozdov and V. M. Kotov, Guanidine: A Simple Molecule with Great Potential: From Catalysts to Biocides and Molecular Glues, *Ineos Open*, 2020, **3**, 200–213.

30 D. Barić, I. Dragičević and B. Kovačević, Design of Superbasic Guanidines: The Role of Multiple Intramolecular Hydrogen Bonds, *J. Org. Chem.*, 2013, **78**, 4075–4082.

31 Q. Jiang, Y. Zhao, X. Zhang, X. Yang, Y. Chen, Z. Chu, Q. Ye, X. Li, Z. Yin and J. You, Surface passivation of perovskite film for efficient solar cells, *Nat. Photonics*, 2019, **13**, 460–466.

32 W. Guo, H. Chen, X. Liu, Y. Ma, J. Wang, Y. Liu, S. Han, H. Xu, J. Luo and Z. Sun, Rational alloying of secondary and aromatic ammonium cations in a metal-halide perovskite toward crystal-array photodetection, *Sci. China Mater.*, 2022, **65**, 179–185.

33 Q. Fan, Y. Ma, H. Xu, Y. Song, Y. Liu, J. Luo and Z. Sun, Near-room-temperature reversible switching of quadratic optical nonlinearities in a one-dimensional perovskite-like hybrid, *Microstructures*, 2022, **2**, 2022013.

34 Z. Xu, Y. Li, X. Liu, C. Ji, H. Chen, L. Li, S. Han, M. Hong, J. Luo and Z. Sun, Highly Sensitive and Ultrafast Responding Array Photodetector Based on a Newly Tailored 2D Lead Iodide Perovskite Crystal, *Adv. Opt. Mater.*, 2019, **7**, 1900308.

35 S. You, P. Yu, J. Wu, Z. K. Zhu, Q. Guan, L. Li, C. Ji, X. Liu and J. Luo, Weak X-Ray to Visible Lights Detection Enabled by a 2D Multilayered Lead Iodide Perovskite with Iodine-Substituted Spacer, *Adv. Sci.*, 2023, **10**, 2301149.

36 Z. Xu, X. Dong, L. Wang, H. Wu, Y. Liu, J. Luo, M. Hong and L. Li, Precisely Tailoring a $FAPbI_3$-Derived Ferroelectric for Sensitive Self-Driven Broad-Spectrum Polarized Photodetection, *J. Am. Chem. Soc.*, 2023, **145**, 1524–1529.

37 G. Maculan, A. D. Sheikh, A. L. Abdelhady, M. I. Saidaminov, M. A. Haque, B. Murali, E. Alarousu, O. F. Mohammed, T. Wu and O. M. Bakr, $CH_3NH_3PbCl_3$ Single Crystals: Inverse Temperature Crystallization and Visible-Blind UV-Photodetector, *J. Phys. Chem. Lett.*, 2015, **6**, 3781–3786.

38 M. I. Saidaminov, A. L. Abdelhady, B. Murali, E. Alarousu, V. M. Burlakov, W. Peng, I. Dursun, L. Wang, Y. He, G. Maculan, A. Goriely, T. Wu, O. F. Mohammed and O. M. Bakr, High-quality bulk hybrid perovskite single crystals within minutes by inverse temperature crystallization, *Nat. Commun.*, 2015, **6**, 7586.

39 D. Shi, V. Adinolfi, R. Comin, M. Yuan, E. Alarousu, A. Buin, Y. Chen, S. Hoogland, A. Rothenberger, K. Katsiev, Y. Losovyj, X. Zhang, P. A. Dowben, O. F. Mohammed, E. H. Sargent and O. M. Bakr, Low trap-state density and long carrier diffusion in organolead trihalide perovskite single crystals, *Science*, 2015, **347**, 519–522.

40 Y. C. Kim, K. H. Kim, D.-Y. Son, D.-N. Jeong, J.-Y. Seo, Y. S. Choi, I. T. Han, S. Y. Lee and N.-G. Park, Printable organometallic perovskite enables large-area, low-dose X-ray imaging, *Nature*, 2017, **550**, 87–91.

41 M. Z. Kabir and S. O. Kasap, Charge collection and absorption-limited sensitivity of x-ray photoconductors:

Applications to a-Se and HgI_2, *Appl. Phys. Lett.*, 2002, **80**, 1664–1666.

42 J. Yu, Y. Qu, Y. Deng, D. Meng, N. Tian, L. Li, J. Zheng, Y. Huang, Y. Luo and W. Tan, Hot-pressed $CH_3NH_3PbI_3$ polycrystalline wafers for near-infrared bioimaging and medical X-ray imaging, *J. Mater. Chem. C*, 2023, **11**, 5815–5824.

43 G. Rikner and E. Grusell, Effects of radiation damage on p-type silicon detectors, *Phys. Med. Biol.*, 1983, **28**, 1261.

44 S. O. Kasap, X-ray sensitivity of photoconductors: application to stabilized a-Se, *J. Phys. D: Appl. Phys.*, 2000, **33**, 2853–2865.

45 L. Zhou, X. Lu, J. Wu, H. Jiang, L. Chen, X. Ouyang and K. M. Lau, Self-Powered Fast-Response X-Ray Detectors Based on Vertical GaN p-n Diodes, *IEEE Electron Device Lett.*, 2019, **40**, 1044–1047.

46 D. Bi, X. Li, J. V. Milić, D. J. Kubicki, N. Pellet, J. Luo, T. LaGrange, P. Mettraux, L. Emsley, S. M. Zakeeruddin and M. Grätzel, Multifunctional molecular modulators for perovskite solar cells with over 20% efficiency and high operational stability, *Nat. Commun.*, 2018, **9**, 4482.

47 Z. Liu, W. Lian, Q. Long, R. Cheng, G. Torrieri, B. Zhang, A. Koivuniemi, M. Mahmoudzadeh, A. Bunker, H. Gao, H. He, Y. Chen, J. Hirvonen, R. Zhou, Q. Zhao, X. Ye, X. Deng and H. A. Santos, Promoting cardiac repair through simple engineering of nanoparticles with exclusive targeting capability toward myocardial reperfusion injury by thermal resistant microfluidic platform, *Adv. Funct. Mater.*, 2022, **32**, 2270201.

48 Y. Song, L. Li, M. Hao, W. Bi, A. Wang, Y. Kang, H. Li, X. Li, Y. Fang, D. Yang and Q. Dong, Elimination of Interfacial-electrochemical-reaction-induced polarization in perovskite single crystals for ultrasensitive and stable X-ray detector arrays, *Adv. Mater.*, 2021, **33**, 2103078.

49 S. Meloni, T. Moehl, W. Tress, M. Franckevičius, M. Saliba, Y. H. Lee, P. Gao, M. K. Nazeeruddin, S. M. Zakeeruddin, U. Rothlisberger and M. Graetzel, Ionic polarization-induced current-voltage hysteresis in $CH_3NH_3PbX_3$ perovskite solar cells, *Nat. Commun.*, 2016, **7**, 10334.

50 Y. Lin, Y. Bai, Y. Fang, Q. Wang, Y. Deng and J. Huang, Suppressed Ion Migration in Low-Dimensional Perovskites, *ACS Energy Lett.*, 2017, **2**, 1571–1572.

